Calibrated 200-GHz Waveform Measurement

Dylan F. Williams, *Fellow, IEEE*, Paul D. Hale, *Senior Member, IEEE*, Tracy S. Clement, *Member, IEEE*, and Juanita M. Morgan

***Abstract*—We develop a method for mismatch-correcting temporal waveforms measured with a high-speed electrooptic sampling system to 200 GHz. The new calibration determines a complete equivalent-circuit model describing the source in both the time and frequency domains with uncertainties, and accounts for all impedances and multiple reflections in the measurement system.**

***Index Terms*—Electrooptic sampling (EOS), mismatch correction, on-wafer measurement, temporal waveform measurement.**

I. Introduction

We develop and demonstrate a novel method of measuring and mismatch-correcting temporal waveforms in a lossy coplanar waveguide (CPW) fabricated on an electrooptic $LiTaO_3$ substrate. We correct our measurements for the complex characteristic impedance and dispersion of the CPW, mismatches, and multiple reflections in the measurement system. These corrections use complex impedance measurements made with an ohmmeter at dc, a vector network analyzer (VNA) to 110 GHz, and a novel and completely noninvasive slotted-line technique above 110 GHz.

Electrooptic sampling (EOS) has been used to characterize printed transmission lines at very high frequencies [1], to measure high-speed waveforms [2] and scattering parameters [3]–[5], and to characterize the invasiveness of electrooptic probes [6]. In [7]–[9], we reported on mismatch-corrected frequency-domain waveform measurements to 110 GHz. We performed all of our impedance measurements in [7]–[9] with a 110-GHz VNA. However, the bandwidth limitation of the VNA prevented us from characterizing our sources, which have significant energy above 110 GHz, in the time domain. Thus, a fully mismatch-corrected characterization of the source in the time domain was not possible.

Here, we develop slotted-line impedance measurements using our noninvasive EOS system. We demonstrate the measurements up to the frequency where the spectrum of the source approaches the noise floor of our instrumentation, approximately 200 GHz in our case. As a result, we can measure and mismatch correct almost all of the energy in the signal. We perform these measurements in CPW because we can excite a single well-defined electromagnetic mode in CPW to frequencies much higher than possible in standard coaxial transmission media.

Using these exceptionally high-speed measurements, we transform our uncorrected measurements to the frequency domain, perform electrical mismatch corrections, and then transform the results back into the time domain. We can recover the time-domain signal accurately because our low noise floor allows us to obtain a 200-GHz measurement bandwidth, which is significantly larger than the roughly 70-GHz bandwidth of the pulse we are measuring.

Manuscript received June 15, 2004; revised September 1, 2004.

The authors are with the National Institute of Standards and Technology, Boulder CO 80305 USA (e-mail: dylan@boulder.nist.gov).

Digital Object Identifier 10.1109/TMTT.2005.845760

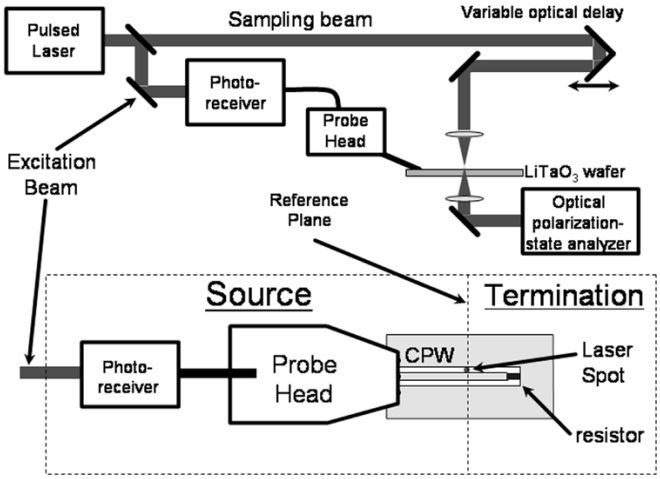

Fig. 1. Sketch of the EOS system. The source consists of the photoreceiver, probe head, and short section of the CPW. The termination consists of a section of the CPW terminated in a planar resistor. Changing the delay of the sampling beam allows us to map out the voltage at the reference plane in the CPW as a function of time. After [7]–[9].

Since our measurements are mismatch corrected, we can accurately compute quantities such as the voltage our on-wafer source would supply to a perfect 50-Ω load in the CPW. Although not the focus of this paper, the method also determines both the frequency-domain and temporal Thévenin and Norton equivalent circuits describing the source [7], and could be used to calibrate other temporal on-wafer measurement systems with bandwidths exceeding those possible in 1-mm coaxial transmission lines.

II. Measurement System

We used the noninvasive EOS system described in [7]–[9] to measure the electrical waveform of an "on-wafer source" in the CPW. This source consisted of a photoreceiver, probe head, and 270-μm section of the CPW before the measurement reference plane.

Fig. 1 sketches the EOS system we used. The mode-locked fiber laser emits a series of short roughly 100-fs optical pulses that are split by the beam splitter into an optical "excitation beam" and an optical "sampling beam." The optical excitation beam excites the photoreceiver, which generates a fast electrical pulse that is coupled onto the CPW line by the wafer probe. This waveform is terminated by a resistive load at the end of the CPW.

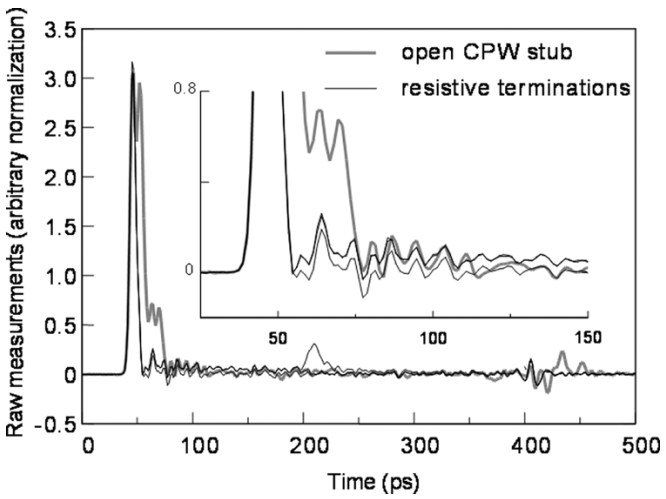

Fig. 2. Uncorrected measurements of the waveform at the CPW reference plane. The pulse at roughly 200 ps is due to the 108-Ω terminating resistor, and is not an artifact of the source. The differentiated pulse at roughly 400 ps is due to multiple reflections inside the source. The inset shows the same measurements on a finer scale.

We use the optical sampling beam to reconstruct the repetitive electrical waveform generated by the source at the on-wafer reference plane in the CPW. We do this by passing the sampling beam through a variable optical delay, polarizing it, and then passing it through one of the gaps of the CPW. Since the $LiTaO_3$ substrate is electrooptic, the electric field between the CPW conductors changes the polarization of the optical sampling beam passing through it. We detect this change, which is proportional to the voltage in the CPW at the instant at which the optical pulse arrived there, with our polarization analyzer without perturbing the electrical signal on the CPW at all. By adjusting the delay in the path of the sampling beam, we adjust the relative time at which the optical pulse in the sampling beam reaches the surface of the substrate. We are thus able to trace out the electrical waveform in the CPW as it evolves with time, as described in [7]–[9].

III. Uncorrected Pulse Measurements

Fig. 2 shows four uncorrected waveforms we measured in the CPW with our EOS system. The thick grey line corresponds to the waveform we measured with the source terminated in a 200-μm open CPW stub. The other three thin black lines correspond to waveforms generated by the source terminated by a 200-μm section of CPW terminated in a resistor with a dc resistance of approximately 37 Ω, by a 5200-μm section of CPW terminated in a resistor with a dc resistance of approximately 37 Ω, and by a 5200-μm section of CPW terminated in a resistor with a dc resistance of approximately 108 Ω.

Even though the source is the same in all four cases, the main pulse as measured with the source terminated in the open CPW stub splits into two pulses approximately 6 ps apart, and is much broader than when the source is terminated in the three resistive terminations. We observed a similar broadening of the pulses in [7] and [8], but could not resolve the splitting in these previous measurements due to the longer duration of the pulses generated by those lower bandwidth sources.

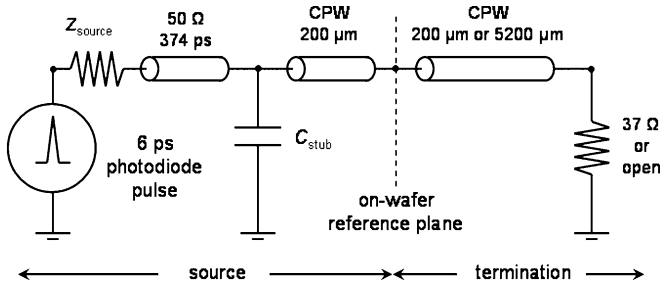

Fig. 3. Equivalent-circuit model for the source and CPW termination.

The waveform with the source terminated in the 5200-μm section of CPW terminated in a resistor with a dc resistance of approximately 108 Ω has a bump at approximately 210 ps, and both waveforms with the source terminated in the longer 5200-μm section of line have small "shoulders" that extend out to approximately 210 ps. Furthermore, while all of the waveforms exhibit a second differentiated pulse at approximately 400 ps, the shape of this pulse differs with the termination employed.

We used the simplified equivalent-circuit model of Fig. 3 to better understand these artifacts of the measurements. The first 50-Ω transmission line in front of the source models the delay between the photoreceiver and the on-wafer reference plane due to the adapters and probe head we employed. We determined the length in the model from 110-GHz reflection coefficient measurements of the photoreciever. From the geometry and dielectric constant of $LiTaO_3$, we estimated $C_{\rm stub}$, the parasitic capacitance associated with the 25-μm section of the CPW underneath the probe tip and its fringing fields, to be approximately 21.5 fF. We determined the characteristic impedance and propagation constant of the CPW from fits to our VNA measurements. We determined the impedance $Z_{\rm source}$ from 110-GHz VNA measurements and approximated the impedance of the on-wafer resistors from their dc resistances. Finally, we set the pulsewidth of the photoreceiver in the model to 6 ps, a value that corresponds well with our uncorrected pulsewidth measurements.

We then used a circuit simulator to evaluate the model of Fig. 3. The simulations agreed remarkably well with our measurements. The delays between the main pulse and the other pulses in our simulations agreed to within roughly 2 ps and the shapes displayed the same trends and features. This allowed us to easily identify the splitting of the main pulse in the open-stub measurement with the reflection of the main pulse off of the open CPW stub, the shoulders with charging and discharging of the lossy CPW in the terminations, and the pulse at 210 ps as due to a reflection off of the 108-Ω resistor. The model also showed that the second differentiated pulse at approximately 400 ps in Fig. 2 is due to a reflection in the source between the photoreceiver and capacitance $C_{\rm stub}$ due to the short section of the CPW under the probe tip.

IV. Impedance Measurements

We used a conventional VNA and an on-wafer multiline thru-reflect-line calibration [10] to measure the reflection coefficients of the source, consisting of the photoreceiver, probe

head, and short section of the CPW, and of our terminations (either the CPW stub or the resistively terminated CPW lines) at our on-wafer reference plane to 110 GHz. This calibration also determines the propagation constant γ of the CPW. We then measured the capacitance C per unit length of the CPW using the short 200-μm section of resistively terminated CPW, as described in [11], and determined the characteristic impedance Z_0 of the CPW from C and γ [12]. Finally, we corrected the reference impedance of our calibration with this measured value of Z_0, as described in [12].

Since our EOS system is entirely noninvasive, we are also able to perform nearly ideal slotted-line measurements in the CPW above 110 GHz without perturbing the electrical signals in the CPW with invasive probes such as those used in [1]–[6]. To perform the slotted-line measurements, we measured the voltage not only at the CPW reference plane in Fig. 1, but also roughly 100 μm to the left- and right-hand side of the CPW reference plane. The frequency-domain voltage $v(z)$ at a position z in the CPW satisfies

$$v(z) = k\left(e^{-\gamma z} + \Gamma_0 e^{\gamma z}\right) \tag{1}$$

where k is a position-independent source term, γ is the propagation constant of the CPW mode, and Γ_0 is the reflection coefficient of the CPW termination at our on-wafer reference plane $(z = 0)$ with respect to a reference impedance of Z_0. This approach rigorously accounts for multiple reflections in the measurements between the CPW terminations and the various discontinuities captured in the reflection coefficient of the source, including reflections in the photoreceiver, probe head, and transition to the CPW line.

In contrast to the reflection coefficients we measured, the relative propagation constant is nearly flat and varies slowly at high frequencies. Thus, to simplify the solution of (1), above 110 GHz, we used extrapolated values of γ measured by our VNA. To perform this extrapolation, we fit the resistance R and inductance L per unit length of our CPW lines to the values of R and L we measured with our VNA below 110 GHz with the heuristic formulas $R = r_0 + r_1 f + r_2 f^{0.6}$ and $L = l_0 + 1_1 f^2 + r_2(1 + f)^{-0.5}$. From these extrapolated values of R and L and our low-frequency value of C, we then estimated γ above 110 GHz. This allowed us to solve for k and Γ_0 in (1) with a straightforward linear least squares fit from our measurements of $v(z)$ performed at our three sampling points separated by roughly 100 μm.

We also used our previously measured values of γ below 110 GHz and previously extrapolated values of γ above 110 GHz to estimate the complex characteristic impedance Z_0 of the lossy CPW and reset the reference impedance to 50 Ω with the methods of [11] and [12]. This allowed us to overcome the approximations of constant real characteristic impedances used in [4] and [5] when calculating reflection coefficients.

Finally, we determined the reflection coefficients and impedances of our on-wafer structures in this way to 375 GHz.[1]

[1]To measure the reflection coefficient of our photoreceiver and probe, we employed a thru line and a second similar photoreceiver and probe at its far end as an electrical source.

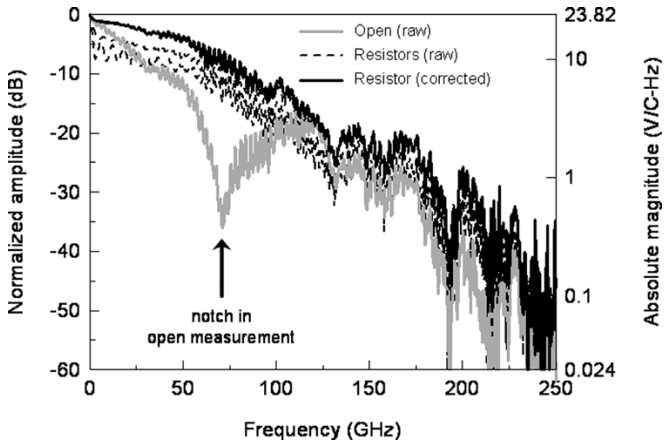

Fig. 4. Fourier transforms of the raw measurements, as well as the corrected measurement for our 200-μm and 37-Ω resistor. The normalized scale on the left-hand side allows the data to be compared easily. The scale on the right-hand side gives the amplitude response of the photoreciever in the CPW generated by a narrow optical pulse that creates one coulomb of charge at the photoreceiver's bias port.

V. Mismatch Correction

We calibrated the overall amplitude response of our EOS system with a 1-kHz sine wave and calibrated ac voltmeter, This procedure relies on the fast response time of the $LiTaO_3$ to transfer this 1-kHz calibration to the other frequencies we measured. We were careful to measure and account for all cable losses in this process.

Since our measurement system is linear and (except during the short time interval during which the photoreceiver is being excited by the optical pulse) time invariant, we are able to represent our measurements in both the time and frequency domains. To mismatch correct the waveforms in Fig. 2, we transformed our temporal measurements to the frequency domain, as illustrated in Fig. 4. This figure shows the Fourier transforms of the measurements in resistively terminated CPW as dashed lines and the measurements in the open CPW stub as a wide grey line.

We then used our impedance measurements to determine the voltage that the source would generate across a perfect 50-Ω load. The corrected data for the 200-μm 37-Ω resistive termination is shown as a black solid line in Fig. 4. Finally, we transformed the frequency-domain results back into the time domain to obtain the four temporal mismatch-corrected impulse responses of our source plotted in Fig. 5.

Fig. 5 shows that the splitting of the main pulse measured with the open CPW stub disappears, and the shoulders and reflection at 250 ps in the uncorrected measurements are absent, confirming that these were artifacts of the terminations, not of the source. The differentiated pulse at roughly 400 ps remains, and the shapes of this pulse after correction are independent of the terminations, confirming that this is, indeed, an attribute of the source, and not of the terminations.

VI. Measurement Bandwidth and Noise Floor

The power in the spectrum of our source reaches the approximately 0.1-V/C $\cdot$ Hz noise floor of our measurement system (see Fig. 4) at approximately 230 GHz. As the signal falls into the

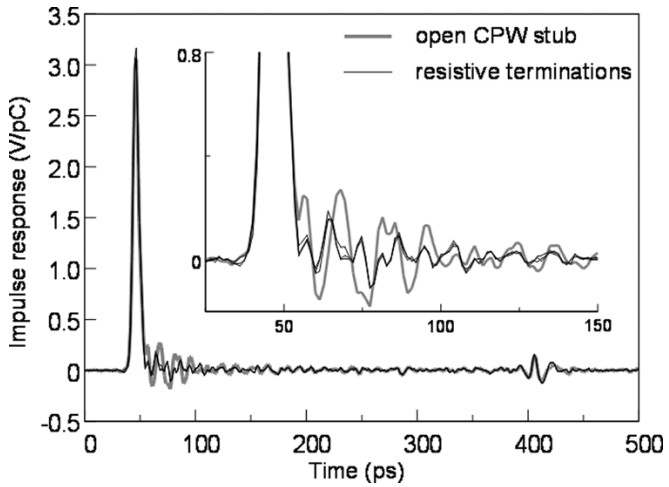

Fig. 5. Corrected waveform measurements at the CPW reference plane. The photons in the short optical input pulse generate charges that are swept out of the photodiode. The plotted quantity corresponds to the voltage the source will generate in the CPW when excited by a narrow optical pulse that generates 1 pC of charge at the photoreceiver's bias port. The inset shows the same measurements on a finer scale.

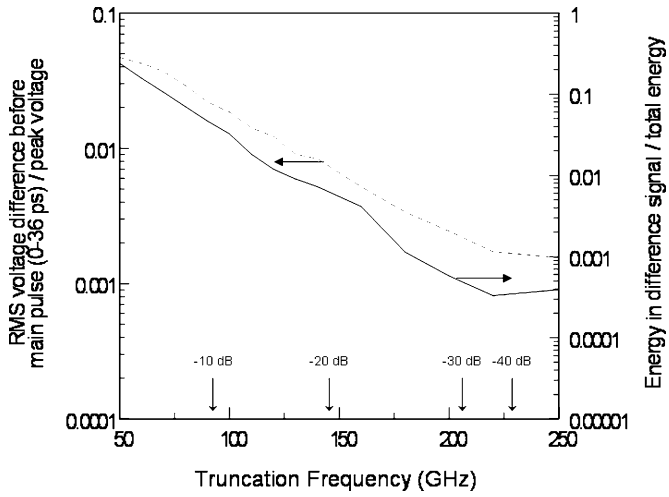

Fig. 6. RMS voltage in the corrected waveforms just before the main pulse arrives (dashed curve) and the ratio of the energy in the difference of the corrected frequency-truncated signal and corrected full-bandwidth signal (solid curve) to the total energy in the signal as a function of the bandwidth used to reconstruct the temporal waveform from its frequency-domain representation. The arrows near the bottom of this figure indicate the approximate drop in the level of the power spectrum of the waveform from its low-frequency value as a function of frequency.

noise, it becomes difficult to measure and our slotted-line reflection-coefficient measurements loose accuracy. Thus, the noise floor of our measurement system, rather than the fundamental response time of the system itself, is the most important factor determining our ability to characterize a high-speed waveform.

Fig. 6 illustrates the importance of achieving a low system noise floor and, thus, capturing as much of the bandwidth and energy in the signal as possible. We first looked at ringing in the corrected waveforms just before the main pulse arrived introduced by truncating the spectrum of the waveform. The dashed curve plots the root mean square (rms) voltage of our corrected waveform between 0–36 ns (just before the arrival of the main pulse) as a function of the bandwidth used to reconstruct the temporal waveform from its frequency-domain representation. As the signal bandwidth is reduced, ringing in the temporal waveform due to truncation of the frequency-domain representation results in significant voltage deviations before the arrival of the main pulse. Since we do not see these voltage deviations in the uncorrected measurement, we believe that this is a good indication of the measurement error between 0–36 ps due to frequency truncation.

The solid curve in Fig. 6 shows the total energy in the difference of the frequency-truncated signal and full-bandwidth signal as a function of the bandwidth used to reconstruct the temporal waveform from its frequency-domain representation. Again, discrepancies in the results grow as the signal bandwidth is reduced, illustrating the importance of obtaining a low measurement-system noise floor for these measurements. Not only do the curves in Fig. 6 flatten out above 250 GHz, but our measurements with 200 GHz or greater bandwidth were nearly identical to our measurements made using the entire 375 GHz of bandwidth.

VII. Measurement Uncertainty

There is an uncorrected residual ripple with a period of roughly 14.7 ps in the open-stub measurements. We attribute this ripple to the difficult-to-correct 25-dB notch in the spectrum of the raw open measurements at 68 GHz shown in Fig. 4. We found it difficult to precisely identify the cause of this 68-GHz notch in the spectrum, but it does appear to be associated with the pulse splitting and shoulder in the 50–80-ns region of Fig. 2.

Except for this residual ripple in the open-stub measurements, the four measurements agree quite well. In fact, it is nearly impossible to distinguish the three mismatch-corrected waveforms performed with the resistive terminations plotted in solid black lines in Fig. 5.

To better quantify our measurement accuracy when using resistive terminations, we constructed a Monte Carlo simulator to estimate the systematic errors in our measurements due to the finite response time of the $LiTaO_3$ substrate, the finite optical pulsewidth and optical beam waist, penetration and spatial variation of the electric field into the substrate, and multiple optical reflections in the substrate, as explained in [7]–[9]. To these errors, we added estimates of the systematic errors due to drift, the determination of C, linewidth and line-length errors, asymmetry in the CPW reflect, and metal nonuniformity in our VNA calibrations, contact resistances in our dc resistance measurements, the accuracy with which we can position the optical beam on the wafer, and variation due to the choice of fitting ranges when extrapolating γ.

While we introduced the systematic measurement errors in the frequency domain, we were careful to preserve the correlations in the errors so that they would correctly transform back into the time domain. As we explained earlier, this approach is based on the linear and time-invariant properties of our measurement system.

This analysis showed that the systematic uncertainty of our open measurement was much larger than the systematic uncertainty of our resistively terminated measurements. This is most

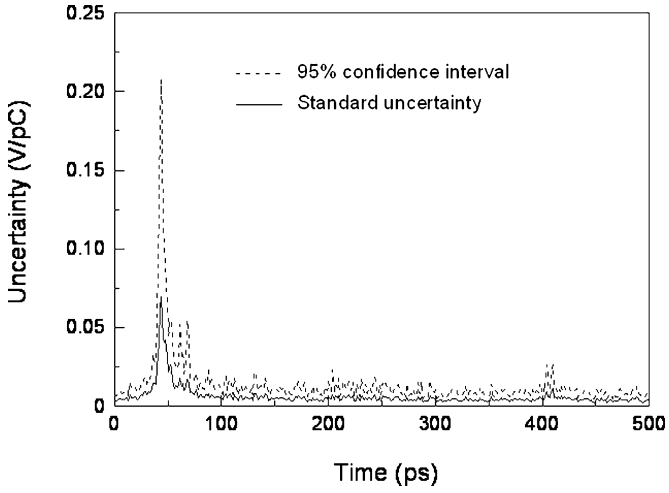

Fig. 7. Standard and expanded 95% uncertainties for the mismatch-corrected and resistively terminated temporal measurements of Fig. 4.

TABLE I
RISE TIME AND PULSE DURATION

Parameter	Value (ps)	Standard uncertainty	95% uncertainty
Rise Time	4.27	0.12	0.33
Pulse Duration	5.96	0.06	0.21

certainly due to difficulty of correcting for the 25-dB notch in the spectrum of the open measurement shown in Fig. 4. Based on this analysis of the systematic uncertainty, we excluded the open from the measurement set. This illustrates an important application of the uncertainty analysis: it can be used as an aid in the selection of the best on-wafer terminations.

We next estimated our uncertainty due to random sources of error (these are not accounted for by our Monte Carlo analysis) from the deviations of the three remaining resistively terminated measured waveforms. We then combined this estimate of our random uncertainty with the estimate of systematic uncertainty from our Monte Carlo simulator to obtain the combined standard uncertainty [13]. We used the Welch–Satterthwaite formula with an infinite number of degrees of freedom for our systematic uncertainty and two degrees of freedom for our random uncertainty to calculate our expanded 95% uncertainty from the standard uncertainties in our measurements, as recommended in [13]. Fig. 7 shows our combined standard uncertainty for the measurements of the source terminated with the resistive terminations in a solid line, and our expanded 95% uncertainty [13] in a dashed line.

Finally, Table I shows our calculations of 10%–90% rise time (first transition duration) and the full-width at half-maximum pulse duration for our source when driving a 50-Ω load. By calculating these quantities for the three resistively loaded waveforms and in our Monte Carlo simulator, we were again able to separately estimate and then combine our random and systematic errors. Table I also shows the combined standard uncertainty and expanded 95% uncertainty for these quantities.

VIII. CONCLUSION

These results have illustrated how useful mismatch corrections can be for accurately characterizing the temporal characteristics of a source from raw waveform measurements. While in this paper we limited our discussion to the waveform the source would supply to a perfect 50-Ω load, it is easy to find either the Thévenin or Norton equivalent circuits for the source from this information [7].

The results also show how mismatch corrections circumvent some of the pitfalls of time-domain gating. For example, without extra analysis, one might have chosen a time-domain window that erroneously gated out the second differentiated pulse in the measurements at about 400 ps.

The measurement method we have developed yields a complete characterization of the impedance and temporal properties of the source. The measurement bandwidth is limited only by the bandwidth of the source. Finally, our measurement uncertainties illustrate the remarkable accuracy of this unique measurement technique.

REFERENCES

[1] M. Y. Frankel, S. Gupta, J. A. Valdmanis, and G. A. Mourou, "Terahertz attenuation and dispersion characteristics of coplanar transmission lines," *IEEE Trans. Microw. Theory Tech.*, vol. 39, no. 6, pp. 910–916, Jun. 1991.

[2] M. Y. Frankel and D. Pavlidis, "An analysis of the large-signal characteristics of AlGaAs/GaAs heterojunction bipolar transistors," *IEEE Trans. Microw. Theory Tech.*, vol. 40, no. 3, pp. 465–474, Mar. 1992.

[3] M. Y. Frankel, "500-GHz characterization of an optoelectronic S-parameter test structure," *IEEE Micro. Guided Wave Lett.*, vol. 4, no. 4, pp. 118–120, Apr. 1994.

[4] M. Y. Frankel, J. F. Whitaker, G. A. Mourou, and J. A. Valdmanis, "Ultrahigh-bandwidth vector network analyzer based on external electro-optic sampling," *Solid State Electron.*, vol. 35, no. 3, pp. 325–332, 1992.

[5] R. A. Dudley, A. G. Roddie, D. J. Bannister, A. D. Gifford, T. Krems, and P. Facon, "Electro-optic S-parameter and electric-field profiling measurement of microwave integrated circuits," NPL, Teddington, U.K., NPL doc., 1998.

[6] M. Y. Frankel, J. F. Whitaker, G. A. Mourou, and J. A. Valdmanis, "Experimental characterization of external electrooptic probes," *IEEE Microw. Guided Wave Lett.*, vol. 1, no. 3, pp. 60–62, Mar. 1991.

[7] D. F. Williams, P. D. Hale, T. S. Clement, and J. M. Morgan, "Mismatch corrections for electro-optic sampling systems," in *56th ARFTG Conf. Dig.*, Nov.–Dec. 30–1, 2000, pp. 141–145.

[8] ——, "Calibrating electro-optic sampling systems," in *IEEE MTT-S Int. Microwave Symp. Dig.*, Phoenix, AZ, May 20–25, 2001, pp. 1527–1530.

[9] T. S. Clement, P. D. Hale, D. F. Williams, and J. M. Morgan, "Calibrating photoreceiver response to 110 GHz," in *15th Annu. IEEE Lasers Electro-Optics Society Conf. Dig.*, Glasglow, U.K., Nov. 10–14, 2002, pp. 877–878.

[10] R. B. Marks, "A multiline method of network analyzer calibration," *IEEE Trans. Microw. Theory Tech.*, vol. 39, no. 7, pp. 1205–1215, Jul. 1991.

[11] D. F. Williams and R. B. Marks, "Transmission line capacitance measurement," *IEEE Microw. Guided Wave Lett.*, vol. 1, no. 9, pp. 243–245, Sep. 1991.

[12] R. B. Marks and D. F. Williams, "Characteristic impedance determination using propagation constant measurement," *IEEE Microw. Guided Wave Lett.*, vol. 1, no. 6, pp. 141–143, Jun. 1991.

[13] B. N. Taylor and C. E. Kuyatt, "Guidelines for evaluating and expressing the uncertainty of NIST measurement results," NIST, Boulder, CO, Tech. Note 1297, 1994.

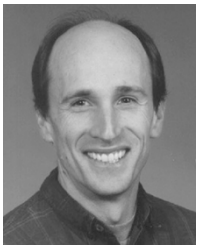

Dylan F. Williams (M'80–SM'90–F'02) received the Ph.D. degree in electrical engineering from the University of California at Berkeley, in 1986.

In 1989, he joined the Electromagnetic Fields Division, National Institute of Standards and Technology (NIST), Boulder, CO, where he develops metrology for the characterization of monolithic microwave integrated circuits (MMICs) and electronic interconnects. He has authored or coauthored over 80 technical papers.

Dr. Williams is an associate editor for the IEEE TRANSACTIONS ON MICROWAVE THEORY AND TECHNIQUES. He was the recipient of the Department of Commerce Bronze and Silver Medals, the Electrical Engineering Laboratory's Outstanding Paper Award, two Automatic RF Techniques Group (ARFTG) Best Paper Awards, the ARFTG Automated Measurements Technology Award, and the IEEE Morris E. Leeds Award.

Paul D. Hale (M'01–SM'01) received the Ph.D. degree in applied physics from the Colorado School of Mines, Golden, CO, in 1989.

Since 1989, he has been a Staff Member with the National Institute of Standards and Technology (NIST), Boulder, CO, where he has conducted research in birefringent devices, mode-locked fiber lasers, fiber chromatic dispersion, broad-band lasers, interferometry, polarization standards, and high-speed opto-electronic measurements. He is currently Leader of the High-Speed Measurements Project in the Sources and Detectors Group, NIST. His research interests include high-speed optoelectronic and microwave measurements and their calibration.

Dr. Hale is currently an associate editor of the JOURNAL OF LIGHTWAVE TECHNOLOGY. He was the recipient of the Department of Commerce Bronze, Silver, and Gold Awards, two automatic RF Techniques Group (ARFTG) Best Paper Awards, and the National Institute of Standards and Technology (NIST) Electrical Engineering Laboratory's Outstanding Authorship Award.

Tracy S. Clement (S'89–M'92) received the Ph.D. degree in electrical engineering from Rice University, Houston, TX, in 1993. Her doctoral research involved the development and study of a variety of ultrashort pulse and very short wavelength lasers.

Since 1998, she has been with the Optoelectronics Division, National Institute of Standards and Technology (NIST), Boulder, CO. Her current research interests include the development of measurement systems for high-speed electrooptic components, as well as ultrashort pulse laser measurements. Prior to joining the Optoelectronics Division, NIST, she was an Associate Fellow of JILA, the Quantum Physics Division, NIST, and was an Assistant Professor Adjoint with the Department of Physics, University of Colorado at Boulder. From 1993 to 1995, she was a Director's Post-Doctoral Fellow with the Los Alamos National Laboratory, Los Alamos, NM.

Juanita M. Morgan was born in Wellston, OH.

She has held research positions with Xicor, Ball Aerospace, and Dynatech Electro-Optics. Since 1990, she has been with the Electromagnetics Division, National Institute of Standards and Technology, Boulder, CO. Her current research interests include processing of high-speed compound semiconductor devices.